remote sensing

MDPI

Article

Interannual Variability of Extreme Precipitation during the Boreal Summer over Northwest China

Qianrong Ma [1], Zhongwai Li [1], Hongjia Lei [1], Zhiheng Chen [2], Jiang Liu [2], Shuting Wang [1], Tao Su [1,*] and Guolin Feng [1,3]

[1] College of Physical Science and Technology, Yangzhou University, Yangzhou 225012, China
[2] Key Laboratory of Meteorological Disaster, Ministry of Education (KLME)/Joint International Research Laboratory of Climate and Environment Change (ILCEC)/Collaborative Innovation Center on Forecast and Evaluation of Meteorological Disasters (CIC-FEMD), Nanjing University of Information Science and Technology, Nanjing 210044, China
[3] China Meteorological Administration Key Laboratory for Climate Prediction Studies, National Climate Center, Beijing 100081, China
* Correspondence: taosu@yzu.edu.cn; Tel.: +86-18151065953

Abstract: Herein, we investigated the characteristics and mechanisms of interannual variability of extreme summer precipitation in northwest China (NWC). The four high-resolution precipitation predicting products under assessment indicated that both the accumulation of summer daily precipitation ≥95th percentile, and the summer maxima of daily precipitation generally decreased in a southeast—northwest direction, while relatively high values were observed in the Tienshan and Qilian Mountain areas. In turn, the Tropical Rainfall Measuring Mission (TRMM) satellite dataset underestimated extreme precipitation in mountainous areas, while Asian precipitation highly—resolved observational data integration towards evaluation (APHRODITE) and Climate Prediction Center (CPC) captured the characteristics of extreme precipitation in NWC. AMIP-type simulations of the interannual variability of extreme summer precipitation in NWC were quite unsuccessful. However, all of them can capture the increasing trends. Therefore, we further found that the interannual increase in extreme precipitation in NWC is strongly correlated with the weakened South Asian high, strengthened Western Pacific Subtropical high, the enhanced westerly jet, and the mid- to high-latitude Rossby wave trains, whose formation and sustenance can be traced back to sea surface temperature-anomalies in the western Pacific in May, June, and July. An increased sea surface temperature promotes convection and induces diabatic heating, which stimulates anticyclonic anomalies that disturb the enhanced westerly jet, resulting in a barotropic Rossby wave train via the Gill-type response. Additionally, it guides more water vapor convergence to NWC and enhances upward motion via anticyclonic anomalies over western Europe and Eastern Asia, and cyclonic anomalies over Central Asia.

Keywords: extreme precipitation; northwest China; Rossby wave trains; western Pacific SST

Citation: Ma, Q.; Li, Z.; Lei, H.; Chen, Z.; Liu, J.; Wang, S.; Su, T.; Feng, G. Interannual Variability of Extreme Precipitation during the Boreal Summer over Northwest China. *Remote Sens.* **2023**, *15*, 785. https://doi.org/10.3390/rs15030785

Academic Editor: Silas Michaelides

Received: 29 December 2022
Revised: 25 January 2023
Accepted: 25 January 2023
Published: 30 January 2023

1. Introduction

In arid and semiarid regions, especially Northwest China (NWC), precipitation is crucial to the hydrological cycle and water resources [1] (Figure 1). With the ongoing global climate change, considerable alterations in the precipitation patterns of this vast area have been observed in recent decades, and wetting and drying trends have become paramount issues for scientific research [2–5]. Thus, for example, Shi et al. (2007) found that, over the last 50 years, the climate in NWC has transitioned from warm and dry to being warmer and wetter [5]. Further, the wet and dry variations that characterize this transition are having devastating impacts on the hydrological cycle, agriculture, water resources, and the ecological environment, all of which have far-reaching consequences for human societies [6–8].

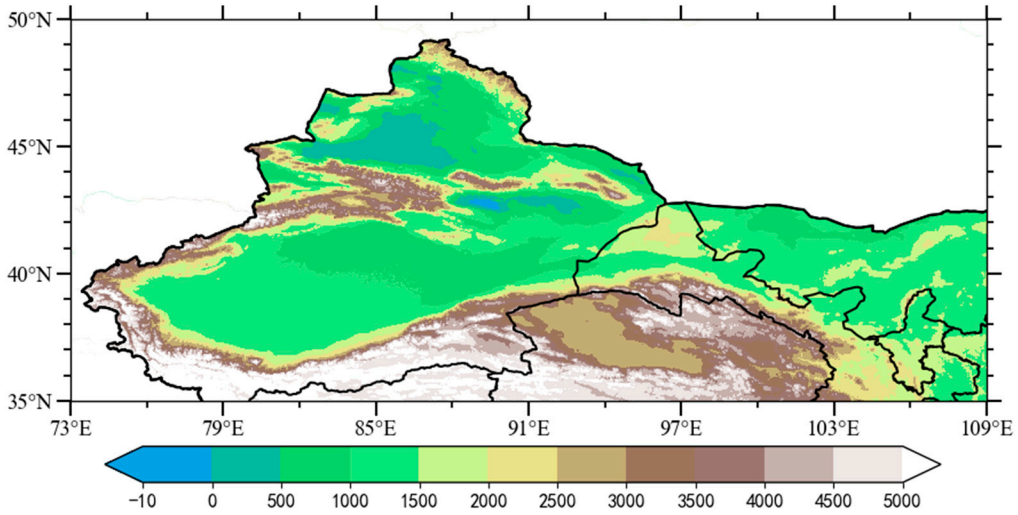

Figure 1. Topographic profile distribution in Northwest China (35°–50°N, 73°–109°E).

According to the assessment report by the Intergovernmental Panel on Climate Change, extreme precipitation has significantly increased in many mid-latitude regions concomitantly with changes in mean total precipitation [9]. NWC is situated in the northern hemisphere's mid-latitudes, in the inner land of the Eurasian continent [10]. Furthermore, both observational evidence and model simulations have confirmed that extreme precipitation events have generally increased in NWC during recent decades, which entail greater risks of flooding, debris flow, and landslides in fragile ecosystems [11,12]. Hence, exploring changes in extreme precipitation events and their possible causes have become an issue of paramount importance for disaster prevention.

Previous studies have shown that, in the context of the ongoing global warming phenomenon, climate shifts in NWC have tended toward warmer—wetter conditions since the 1980s as precipitation has increased more than evaporation [13,14]. Furthermore, melting glaciers, diminishing snow covers, and expanding lake areas have all intensified precipitation in NWC due to the increase in water vapor supply into the atmosphere [15–17]. Specifically, the increasing levels of summer insolation might have been playing a crucial role in the increase in precipitation in NWC during the mid- and late-Holocene [18], together with associated circulatory systems that have also been reported. Thus, precipitation in NWC is mainly controlled by the westerlies [19]; however, in recent decades, water vapor fluxes from the south and southeast dominate summer precipitation in NWC, while the long-term average water vapor content is primarily from the west [20]. Anomalies in atmospheric water vapor in this region are closely associated with the teleconnection patterns, both zonal and meridional, along the Asian westerly jet [2,20–23]. For instance, the pronounced Pacific North America-Eurasian (PNA-EU)-like pattern in the Northern Hemisphere, North Atlantic Oscillation (NAO), and Arctic Oscillation (AO)-like patterns can cause precipitation to increase [24–26]. Consistently, Zhao et al. (2014) reported that circulation anomalies over central Asia promote the subtropical westerly jet (SWJ) southward displacement which promotes a southerly and ascending motion over NWC, enhancing summer precipitation [27]. A weakened south Asian summer monsoon could result in the southeastward shift of the South Asian high (SAH) and the associated anomalous atmospheric circulation will produce anomalous updrafts over the western Asian westerly jet stream, which promotes more summer precipitation in NWC [28]. Thereafter, the Indian Ocean and mid-latitude North Atlantic Sea surface temperature (SST) anomalies and the El Niño–Southern Oscillation (ENSO) have been closely correlated with NWC precipitation patterns [24,29–31]. Yin and Zhou (2020) found that the enhanced negative relationship between ENSO and mid-latitude North Atlantic SST since the mid-1990s can excite a Pacific-North American–Eurasian-like pattern independently, causing significant precipitation anomalies in NWC [24]. Zhou et al. (2015) proposed that the warming SSTs in Indian

Ocean in spring can excite a negative anomaly cyclone at 500 hPa geopotential height, which sustains over the tropical Indian Ocean and then transports water vapor to central Asia which can affect the summer precipitation in Xinjiang [29]. In addition to circulation systems, atmospheric water vapor content is one of the most important factors affecting precipitation in arid and semiarid regions. Summer water vapor in the atmosphere in arid areas is influenced by typhoons and the westward movement of the West Pacific Subtropical high (WPSH) [32], which leads to even more extreme precipitation events occurring in the more arid areas of NWC [33]. Indeed Yao et al. (2016) noted that the arid and semiarid NWC has experienced a substantial increase in water vapor pressure in recent decades, especially in northwestern Xinjiang and the northwestern Hexi Corridor [34]. Similarly, extreme precipitation trends in the mountainous and oasis areas of NWC have increased remarkably in recent decades [35,36]. In addition, the spring surface sensible-heat-flux in NWC, which is related to precipitation changes, and significantly influences summer precipitation in China [37]. Further, Leung and Zhou (2018) emphasized that the anomalous negative center over NWC is concurrent with circumglobal teleconnection, such as the Silk Road and Europe—China patterns. Extreme precipitation in NWC and other arid and semiarid regions is also enhanced by the long-term changes in regional and circumglobal circulations [38,39]. All these previous studies have proposed several factors as possible causes to account for the increase in precipitation in NWC. Here, we have reviewed the contribution of atmospheric circulation to the variation in extreme precipitation, because unraveling these issues is most necessary to thoroughly understand the observed variability and to develop reliable predictors and simulation models to accurately forecast extreme precipitation events.

Therefore, in this study, we focused on detecting the changes in extreme summer precipitation in the arid and semiarid NWC region. Specifically, different datasets were used to examine and describe the detailed variations in summer extreme precipitation in NWC; based on which, the fundamental physical process affecting the key circulation systems and influencing the summer extreme precipitation in NWC were analyzed. Unraveling these issues will help us to better understand the climate changes in NWC and search for reliable predictors of summer extreme precipitation.

2. Materials and Methods

2.1. High-Resolution Precipitation Products

In this study, we first evaluated three widely used high-resolution precipitation products and one satellite-based product.

(1) The gridded daily precipitation data set from 1961–2021 with a resolution of 0.25° latitude × 0.25° longitude, CN05.1, were interpolated using more than 2400 meteorological observation stations in China, which were developed by the National Climate Center and the China Meteorological Administration [40].

(2) The daily Asian precipitation highly-resolved observational data integration towards evaluation (APHRODITE) product developed by the Research Institute for Humanity and Nature (RIHN), Japan, and the Meteorological Research Institute of the Japan Meteorological Agency (MRI/JMA), was created from dense rain-gauge data by interpolating the ratio of the station value to climatology [41]. We used V1901, the latest version, with a spatial resolution of 0.25° latitude × 0.25° longitude on the available data, i.e., during 1998–2015 (http://aphrodite.st.hirosaki-u.ac.jp/products.html (accessed on 20 June 2021)).

(3) The Climate Prediction Center (CPC) of the National Oceanic and Atmospheric Administration (NOAA) has also provided daily high-resolution precipitation data, from 1979 to the present, with a resolution of 0.5° latitude × 0.5° longitude. The CPC collects daily precipitation data from the River Forecast Centers (RFC), the Hydrologic Automated Data System (HADS), the observed Climate Anomaly Monitoring System (CAMS), and the National Weather Service (NWS). National collections from meteorological agencies in Mexico and countries in South America, East

Asia, and Africa were also used. The objective analysis technique of optimum interpolation utilized to create a suite of unified precipitation products is available https://www.psl.noaa.gov/data/gridded/data.cpc.globalprecip.html (accessed on 1 January 2023)) [42].

(4) Besides the aforementioned products, we used satellite daily Tropical Rainfall Measuring Mission (TRMM) 3B42-V7 precipitation data with a spatial resolution of 0.25° latitude × 0.25° longitude. An optimal combination of the TRMM Microwave Imager (TMI), Special Sensor Microwave Imager (SSM/I), Advanced Microwave Scanning Radiometer (AMSR), and Advanced Microwave Sounding (AMSU) were employed to reproduce the TRMM 3B42-V7 product. Due to the limitation of remote sensing technology in high-altitude and complex terrain areas, their results may have biases. Unfortunately, this product only covers regions from 180°W to 180°E and 50°S to 50°N during the years 1998–2019 (https://disc.gsfc.nasa.gov/datasets/TRMM_3B43_7 (accessed on 23 November 2021)) [43].

2.2. Other Datasets

This study used seven historical simulations of the Coupled Model Intercomparison Project Phase 6 (CMIP6) experiment [44] simultaneously. The details of the data structures and information are shown in Table 1. In order to gain an understanding of the factors related to extreme precipitation in NWC, the daily and monthly reanalysis data ERA5 used in this study were provided by the European Center for Medium-Range Weather Forecasts (ECMWF), which has a horizontal resolution of 0.25° latitude × 0.25° longitude [45]. In addition, monthly mean SST data were derived from the Hadley SST dataset (HadISST) with a horizontal resolution of 1.0° latitude × 1.0° longitude from 1961 to 2021 [46].

Table 1. Model names, modeling centers and countries, and spatial resolutions of seven CMIP6 global climate models.

Model Name	Modeling Center and Country	Spatial Resolution (lon × lat)
BCC-CSM2-MR	Beijing Climate Center, China Meteorological Administration (China)	1.125° × 1.1°
FGOALS-g3	LASG, Institute of Atmospheric Physics, China Academy of Sciences and Center for Earth System Science, Tsinghua University (China)	2.25° × 2°
GFDL-CM4	NOAA-Geophysical Fluid Dynamics Laboratory (USA)	1.25° × 1°
GFDL-ESM4	NOAA-Geophysical Fluid Dynamics Laboratory (USA)	1.25° × 1°
MPI-ESM1-2-HR	Max Planck Institute for Meteorology (Germany)	0.9° × 0.9°
MRI-ESM2-0	Meteorological Research Institute (Japan)	1.125° × 1.1°
NESM3	Nanjing University Information Science and Technology (China)	1.875° × 1.9°

2.3. Methods

Research on extreme weather and climate uses precipitation indices provided by the World Meteorological Organization (WMO) Expert Team on Climate Change Detection and Indices (ETCCDI; http://etccdi.pacificclimate.org/list_27_indices.shtml (accessed on 1 January 2023)) [39]. Herein, considering the unique climate characteristics of NWC, we used the value of the 95% percentile of wet days in summer as extreme precipitation. The total summer precipitation accumulations for the days with daily precipitation exceeding the 95th percentiles were defined as R95TOT. The summer maxima of daily precipitation were denoted by Rx1day.

Several statistics were used to quantify similarity among precipitation products over NWC, including the Pearson's correlation coefficient, root–mean square error (RMSE), normalized root–mean square error (NRMSE), and mean relative error (MRE). In turn, Student's *t*-test was used to test the significance of the correlation coefficients. Interdecadal features were isolated using a 9-year running. Additionally, we used an empirical orthogonal function (EOF) to analyze the spatiotemporal characteristics of extreme precipitation in NWC [47]. Furthermore, the influence of meteorological factors on extreme precipitation was explored using linear trends and regression. The South Asian high (SAH) indices were

calculated according to Huang et al. (2011) [48], and the Western Pacific Subtropical high (WPSH) was calculated based on Sui et al. (2007) [49].

Trenberth (1991) proposed a method for calculating the vertical integrated water vapor transport flux (WVT) from the surface to 300 hPa [50]:

$$Q_u = -\frac{1}{g}\int_{p_x}^{p_t} uqdp$$

$$Q_v = -\frac{1}{g}\int_{p_x}^{p_t} vqdp$$

where q, u, v and g represent specific humidity, the zonal winds, the meridional winds, and the acceleration due to gravity, respectively. Pressure (p) ranged from the surface (p_x) to 300 hPa (p_t).

To diagnose the Rossby wave-train energy dispersion characteristics, the wave activity flux (WAFs) was calculated according to Takaya and Nakamura (2001) [51]:

$$W = \frac{1}{2|\overline{U}|}\begin{bmatrix} \overline{u}\left(\psi_x'^2 - \psi'\psi_{xx}\right) + \overline{v}\left(\psi_x\psi'_y - \psi'\psi_{xy}\right) \\ \overline{u}\left(\psi'_x\psi'_y - \psi'\psi'_{xx}\right) + \overline{v}\left(\psi_y'^2 - \psi'\psi'_{yy}\right) \end{bmatrix}$$

where the overbar and prime indicate the climatological mean and anomaly, respectively; ψ denotes the stream function, U is the horizontal wind, and W represents the two-dimensional WAFs of the Rossby wave.

3. Results

3.1. Evaluation of Precipitation Products in NWC

The selected high-resolution precipitation products showed the main characteristics of the spatial distributions of summer R95TOT and Rx1day in NWC (Figure 2). Both R95TOT and Rx1day generally decreased in a southeast—northwest direction and there were relatively high values in the Tienshan and Qilian Mountain areas. For CN05.1, the maximum and minimum values of R95TOT were 138.12 and 9.25 mm, respectively (Figure 2a). The spatial distribution of R95TOT obtained from the other datasets generally agreed with that of CN05.1 (Figure 2b–d). However, it is worth noting that the TRMM product underestimated R95TOT in the Tienshan mountain area, which is limited by the application of remote sensing technologies in high topography areas [52].

Overall, the spatial patterns of R95TOT obtained from applying CPC and APHRODITE were similar to that of CN05.1 (Figure 2c). Similarly, the four precipitation datasets generally captured the spatial characteristics of Rx1day in NWC. As can be seen in Figure 2e, Rx1day generally decreased from the southeast to the northwest and reached a maximum in mountainous areas (ranging from 1.2 to 48.3 mm, Figure 2e–h). However, the TRMM product also underestimated the intensity of extreme precipitation in NWC (Figure 2h). Figure 2i,j shows the standard time series of the regionally averaged R95TOT and Rx1day in NWC. Generally, the four high-resolution precipitation products indicated that R95TOT has increased in recent years (Figure 2i). The correlation coefficients for the different datasets from 1998 to 2015 are further discussed. The correlation coefficients between APHRODITE, CPC, TRMM, and CN05.1 were 0.76, 0.90, and 0.70 (>99% significance level). Rx1day in NWC also showed increasing trends for different precipitation products (Figure 2j), and the correlation coefficients among APHRODITE, CPC, TRMM, and CN05.1 were 0.83, 0.94, and 0.79 (>99% significance level). Among the four high-resolution precipitation products, TRMM tended to underestimate summer extreme precipitation in NWC, as its accuracy is generally unsatisfactory for high-altitude and complex terrain conditions [52]. In contrast, CN05.1 and CPC described extreme precipitation more accurately, showing that its intensity has increased in recent years.

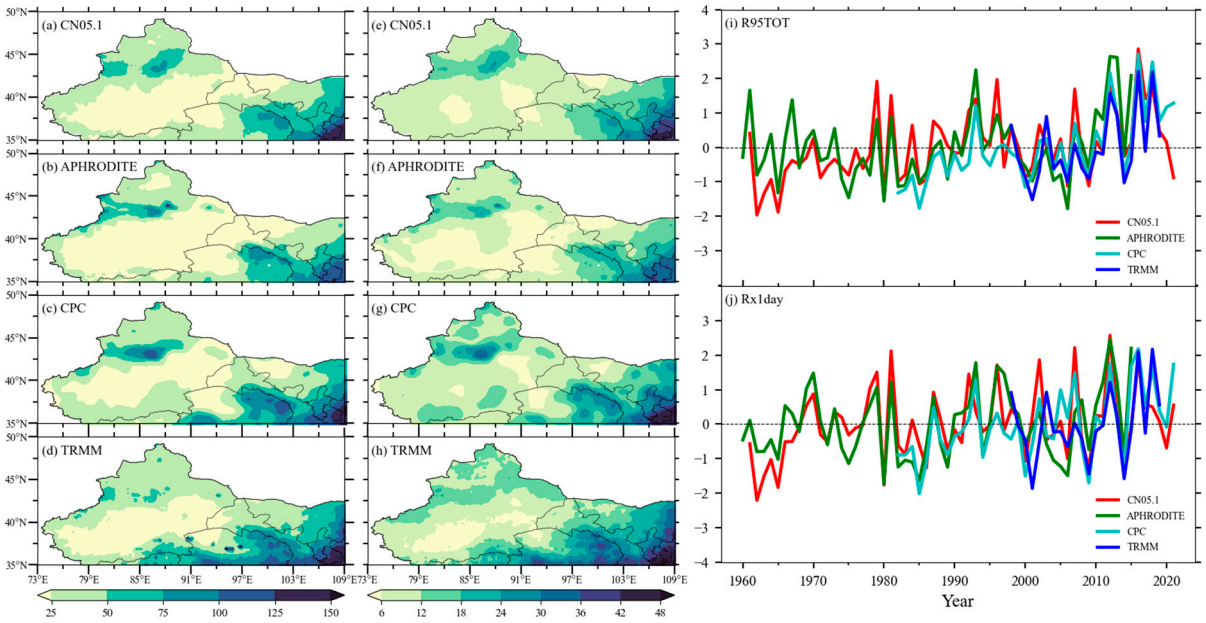

Figure 2. Spatial distributions of R95TOT and Rx1day for (**a**,**e**) CN05.1, (**b**,**f**) Asian precipitation highly-resolved observational data integration towards evaluation (APHRODITE), (**c**,**g**) Climate Prediction Center (CPC), and (**d**,**h**) TRMM in Northwest China (NWC) from 1998–2015 (unit: mm). The standard time series of regional averaged (**i**) R95TOT and (**j**) Rx1day in NWC are shown.

Regardless of general previous knowledge of summer extreme precipitation in NWC, CMIP6 model simulations of the interannual variability of extreme precipitation in NWC were not successful (Figure 3). According to the Taylor diagrams of R95TOT and RX1day in Figure 3a,c, CMIP6 models performed better for RX1day than actual observations. GFDL-CM4 and FGOALS-g3 had higher correlations, lower standard deviation ratios, and lower central root mean square errors; however, in terms of intensity or fluctuation, neither one captured the variability of extreme precipitation in NWC. Furthermore, they appeared to be overestimated (Figure 3b,d). In turn, CMIP6 historical precipitation simulations were driven by historical SST, and state-of-the-art atmospheric general circulation models adjusted for the interannual variability of extreme precipitation in NWC were ineffective in this case. Therefore, a detailed understanding of the dynamic origins of extreme precipitation in NWC is required. Key circulation systems and their fundamental physical processes are critical for improving simulation models and extreme precipitation forecasting.

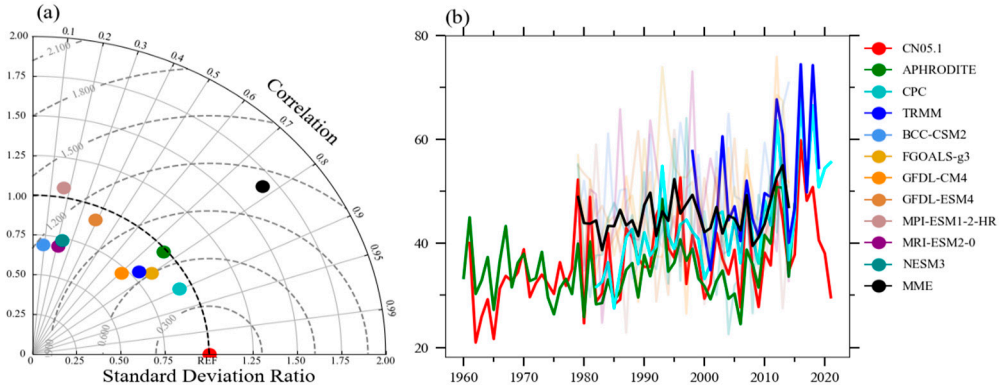

Figure 3. *Cont.*

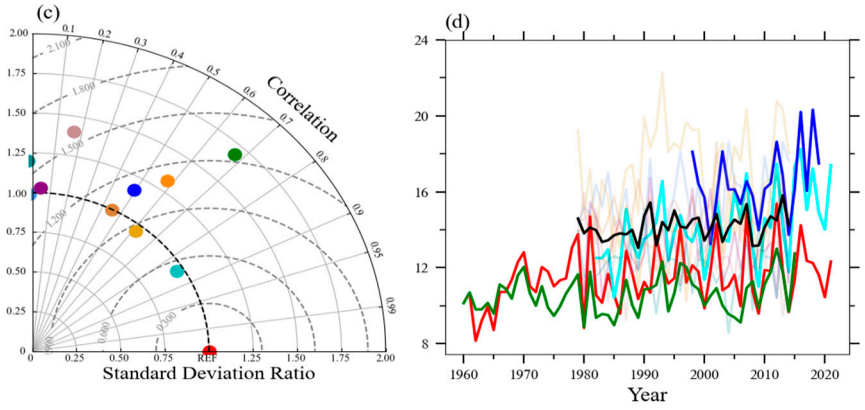

Figure 3. (**a**,**b**) Taylor diagrams and (**c**,**d**) spatially averaged R95TOT and Rx1day. Daily precipitation compared between CMIP6 models and observations are for the years 1998–2014 in NWC.

3.2. Spatiotemporal Features of R95TOT in NWC

Values for R95TOT generally increased in a northwest—southeast direction and were high in the Tienshan and Qilian Mountain areas (Figure 4a). During the years 1961–2021, R95TOT in NWC showed a homogeneous increasing pattern (Figure 4b). The maximum positive was located in the areas of the Tienshan and Qilian Mountains, Pamirs, and southeast NWC, which is consistent with the distribution of precipitation in this region, and with the results of Hu et al. (2019) and Yao et al. (2022). Figure 4c shows the time series of the area-averaged R95TOT in NWC. As can be seen, R95TOT showed significant variability for both interannual and interdecadal time scales. Furthermore, the interannual and interdecadal components accounted for 58% and 42% of the total variance, respectively. Particularly, the interdecadal increase of summer R95TOT in NWC has occurred since the late 1980s, which is consistent with the findings of previous studies and is associated with interdecadal change in moisture flux transport since the late 1980s [37,53].

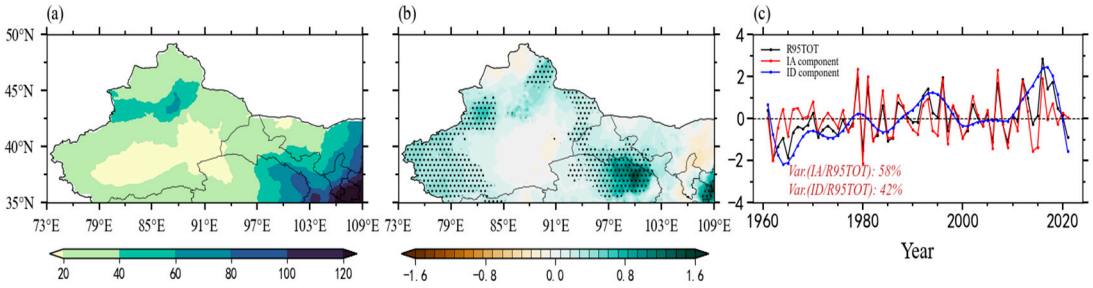

Figure 4. Spatial distributions ((**a**), unit: mm) and linear trend ((**b**), unit: mm year^{-1}) of R95TOT in NWC. Dotted areas indicate significant values at the 95% confidence level based on the Student's *t*-test. (**c**) Time series of normalized year-to-year R95TOT in NWC (black line) and its interannual (red line) and interdecadal (blue line) components during the years 1961–2021.

3.3. Anomalous Atmospheric Patterns for Interannual R95TOT in NWC

Consistent changes in atmospheric circulation are associated with changes in interannual summer extreme precipitation in NWC. Figure 5 shows the atmospheric circulation patterns in summer regressed onto the interannual R95TOT component for the period between 1961 and 2021.

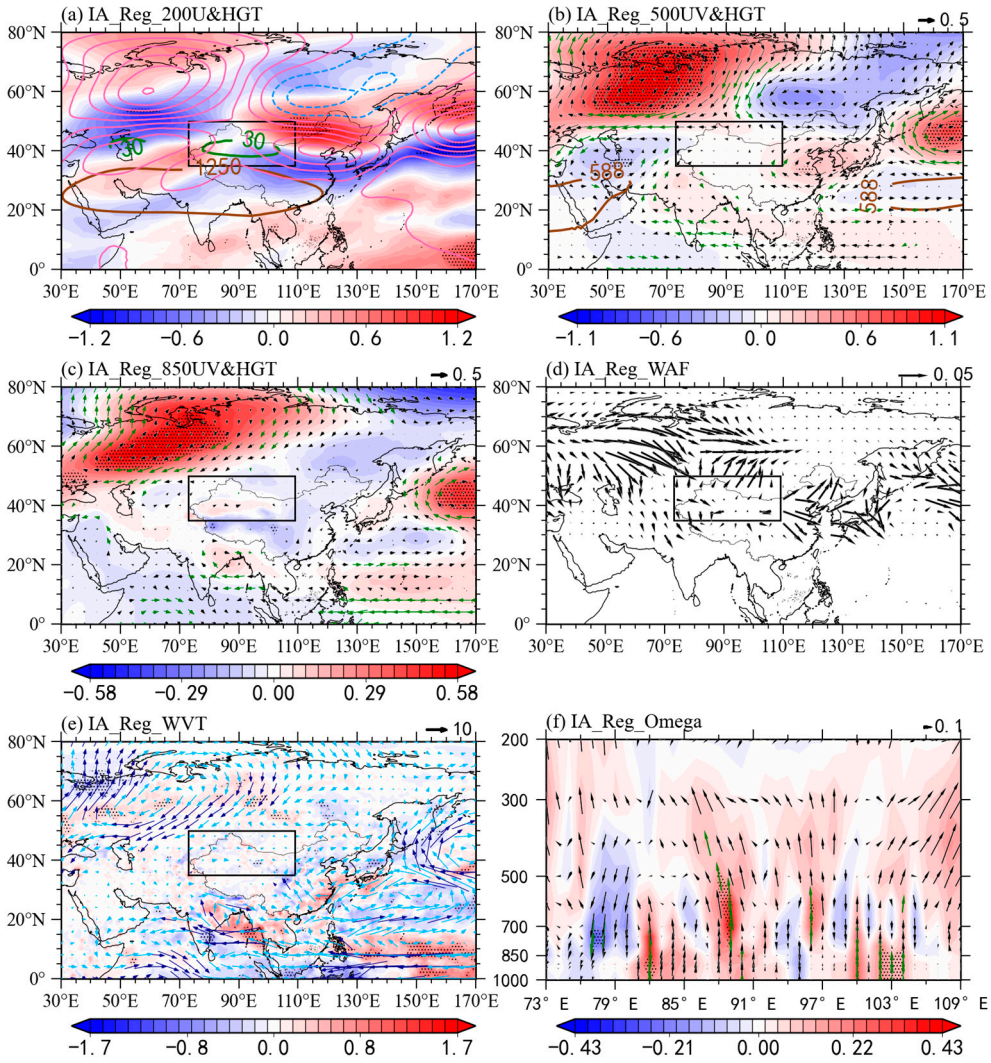

Figure 5. Regressed (**a**) 200 hPa zonal wind (shading; unit: gpm) and geopotential height (contours; unit: gpm), (the solid green lines represent the westerly jet in climatological mean, the solid brown line is the same as the green lines but for the 12,500 isolines at 200 hPa, the solid pink lines and the dashed blue lines represent geopotential height anomaly at 200 hPa), (**b**) 500 hPa wind field (vectors; unit: m s^{-1}) and geopotential height (shading; unit: gpm), (the solid brown lines are the 5880 isolines in climatological mean), (**c**) 850 hPa wind field (vectors; unit: m s^{-1}) and geopotential height (shading; unit: gpm), (**d**) 200 hPa WAFs (vectors; unit: m^2 s^{-2}), and (**e**) integrated water vapor transport flux (WVT) (vectors; unit: kg m^{-2} s^{-1}) and its divergence (shading; unit: 10^{-5} kg s^{-1}) and (**f**) vertical velocity ω (shading; unit: 10^{-2} Pa s^{-1}) and wind field (vectors, unit: m s^{-1}) along the latitudes 35°–50°N in summer onto the interannual component of R95TOT in NWC from 1961 to 2021, respectively. Dotted areas, green vectors, and deep-blue vectors in (**e**) are statistically significant at the 95% confidence level.

Clearly, there were two significant anomalous anticyclonic systems located over western Europe and northeastern China from 200 hPa (Figure 5a) to 500 hPa (Figure 5b), with NWC between the two high-pressure systems. This was accompanied by a strengthened westerly jet at 200 hPa (Figure 5a) and a weakened SAH. Additionally, there is a well-organized tripole pattern of geopotential height at 500 hPa, and the western portion of NWC exhibits a significant negative center and two positive centers in western Europe and northeast China (Figure 5b). Similar patterns were also found at 850 hPa, except for the Tarim Basin. Most of NWC was influenced by anomalies of negative geopotential height, indicating a quasi-barotropic effect (Figure 5c). Specifically, a wave-like teleconnection can be observed over the Eurasian continent, with convergence-divergence–

convergence–divergence WAFs anomalies located over western Europe, Central Asia, NWC, and northeastern Asia (Figure 5d). This anomalous pattern is similar to the conventional EU teleconnection pattern's negative phase [54]. The horizontal WAFs display the propagation of the teleconnection pattern from the North Atlantic, spreading through Eurasia, and convergent at NWC. Meanwhile, anomalies of anticyclonic winds in western Europe, the Bay of Bengal, and eastern China favor moisture flux transport to the NWC from the northern, southern, and eastern boundaries (Figure 5e). Thus, the coherent, negative, anomalous geopotential height-center from 850 to 200 hPa and the abundant water vapor transport favor the severity of extreme precipitation in NWC. The results of the regression analysis of vertical motion against the interannual R95TOT component further indicated that extreme precipitation over NWC was accompanied by a significant upward vertical motion over NWC, which clearly promoted and sustained extreme precipitation in NWC (Figure 5f).

3.4. Impacts of the Western Pacific SST on Interannual R95TOT in NWC

The possible causal factors of the atmospheric circulation anomalies discussed in previous sections for extreme precipitation events over NWC were further investigated aiming to gain a better understanding of these types of events and enhance our ability to forecast extreme meteorological events. Previously, Yin and Zhou (2021) indicated that the North Atlantic SST anomalies and the El Niño–Southern Oscillation are closely related to precipitation in NWC. Meanwhile, warmer SST in the Indian Ocean via anomalous ascending motions and water vapor transport influence extreme precipitation in NWC [55]. Therefore, we analyzed the relationship between SST and the interannual R95TOT.

Figure 6 shows the regressed detrended SST in MJJ against the interannual component of summer R95TOT in NWC from 1961 to 2021. In Figure 6a, the increased extreme precipitation in NWC is accompanied by positive SST anomalies in the western Pacific. We asked whether the anomalous western Pacific positive SST plays a vital role in forcing atmospheric circulation. To answer this question, we calculated the western Pacific positive SST index (SSTI: 2–22°N, 117–135°E). Figure 6b shows the detrended and original SSTI from 1961–2021. As can be appreciated, SSTI shows obvious interannual variability, and the detrended and original SSTI are generally in phase. The correlation coefficient between the interannual R95TOT and the detrended SSTI was 0.44 (exceeding the 99% confidence level) for the entire period. In addition, SSTI increased more markedly from 1997 to 1998, and the correlation with interdecadal R95TOT significantly reached 0.68 at the 99% confidence level. Further, the correlations between SSTI and R95TOT show that extreme precipitation in NWC has a very close relationship with SSTI over the period between 1961 and 2021.

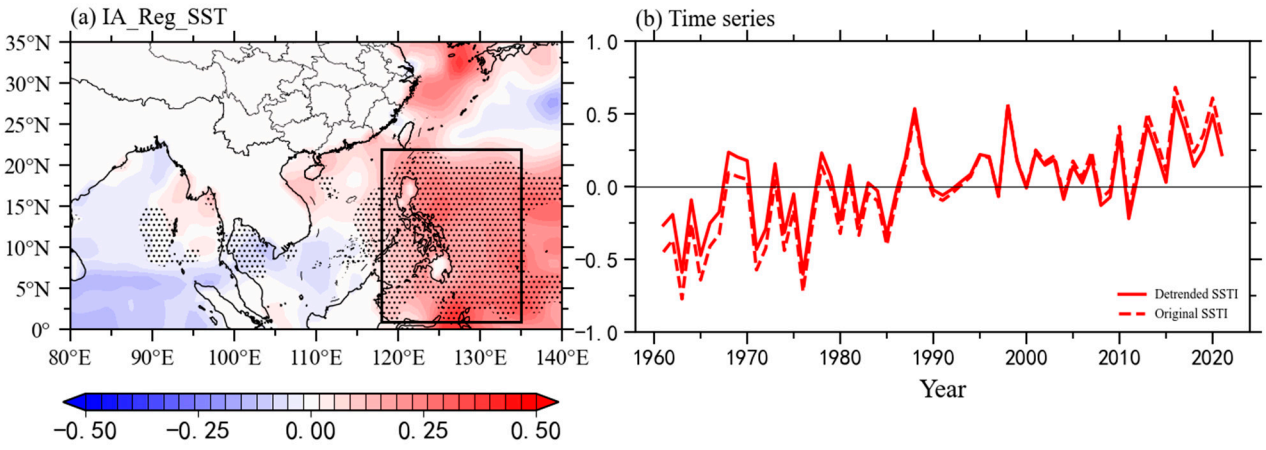

Figure 6. (**a**) Regression maps of SST (shading; unit: °C) in MJJ with regard to the interannual component of summer R95TOT in NWC. Dotted regions represent regression coefficient significance at the 95% confidence level based on Student's *t*-test. (**b**) Standardized time series of the detrended and original SSTI in MJJ from 1961 to 2021.

Figure 7 further shows the regression maps of SSTI in MJJ against the interannual summer R95TOT in NWC. Clearly, positive SST anomalies over the western Pacific have a close relationship with increased extreme precipitation, as there are similar circulation anomalies. Anomalous anticyclonic patterns occurred over western Europe and eastern Asia from 200 (Figure 7a) to 500 hPa (Figure 7b). NWC is located between two high pressure systems and the western and eastern regions are influenced by anomalous cyclonic patterns over Central Asia and Mongolia (Figure 7b,c). The westerly jet at 200 hPa is also enhanced, the SAH weakened, and the WPSH is westwardly enhanced. Increased SSTI promotes convection and induces diabatic heating and stimulates the anticyclonic anomaly, which favors the westerly jet and the WPSH via the Gill-type response [56]. Furthermore, a wave-like teleconnection can be seen over the Eurasian continent, which is similar to that in Figure 5d. The horizontal WAFs' convergence occurred in NWC and increased extreme precipitation events. Figure 5e illustrates WVT anomalies along with an apparent anomalous anticyclonic movement over western Europe with integrated water vapor transport to the northern boundary of NWC. The cyclonic anomaly over the Arabian Sea and the anticyclonic anomaly over the western Pacific are favorable for WVT to the southwestern and eastern boundary of NWC. Thus, abundant WVT converges in NWC and plays an essential role in enhancing extreme precipitation events. Meanwhile, a uniform, upward and significant vertical motion over 79°–100°E promotes extreme precipitation in NWC according to regression of vertical motions.

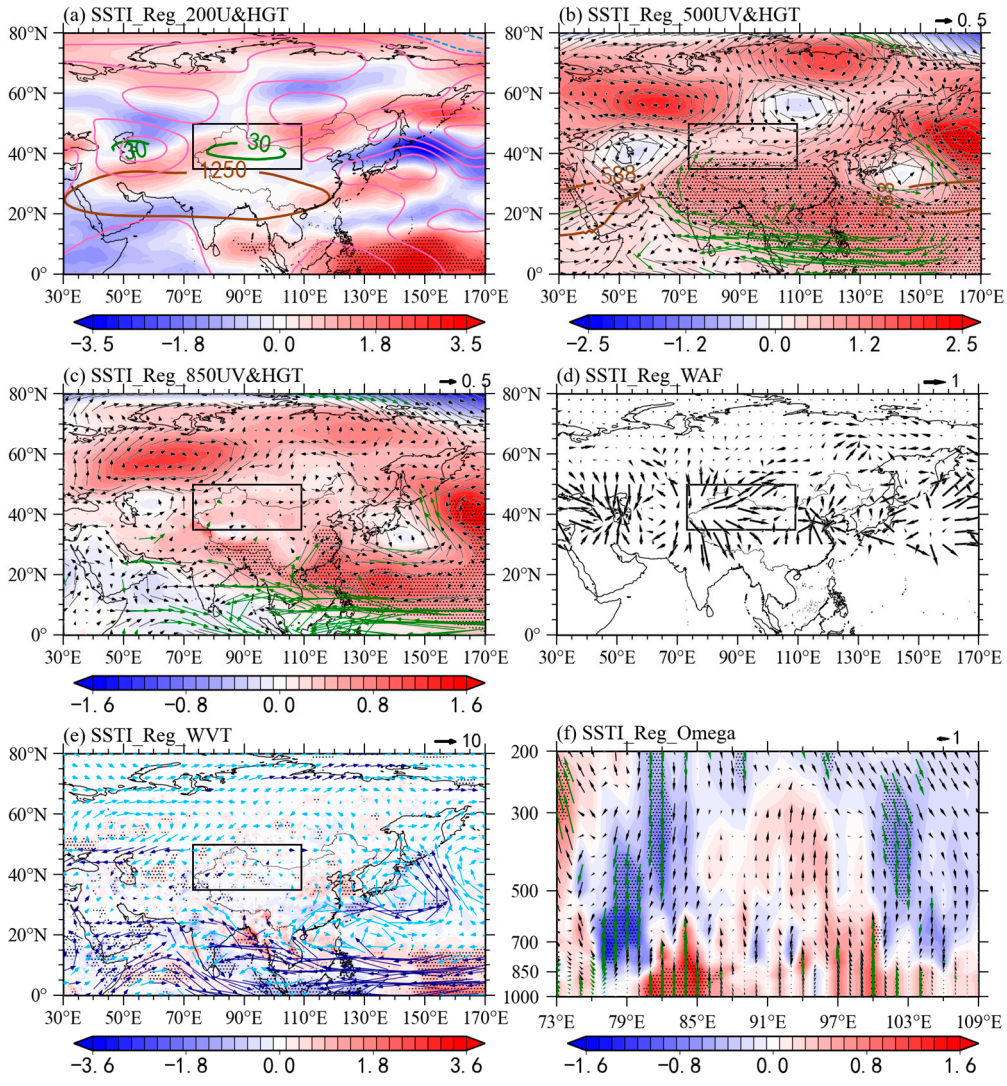

Figure 7. The same as Figure 4, but for sea surface temperature index (SSTI).

Positive SST anomalies likely favor a wave-like train propagating and guiding more water vapor to NWC. These anomalous atmospheric circulations can be sustained from MJJ to JJA and contribute to the frequent extreme precipitation in NWC (Figures 1 and 2). We also found that WPSH intensity and the western ridge point were strengthened by the occurrence of extreme precipitation, which was accompanied by a decrease in the SAH. Figure 8 further illustrates the correlation between a summer WPSH, SAH, and extreme precipitation in NWC. Consistent with the observed results, the strengthened and western-stretched WPSH significantly correlated with increased extreme precipitation in NWC (Figure 8a,b), with correlation coefficients of 0.33 and 0.41 (above the 99% confidence level). It is worth noting that the WPSH changes play a more important role in the interdecadal-increased R95TOT. Meanwhile, reduced the SAH intensity also benefits R90TOT, and the correlation coefficient between the reduced SAH intensity and R90TOT reached −0.28 at the 99% confidence level. Clearly, the SAH intensity has an impact on interannual R95TOT changes.

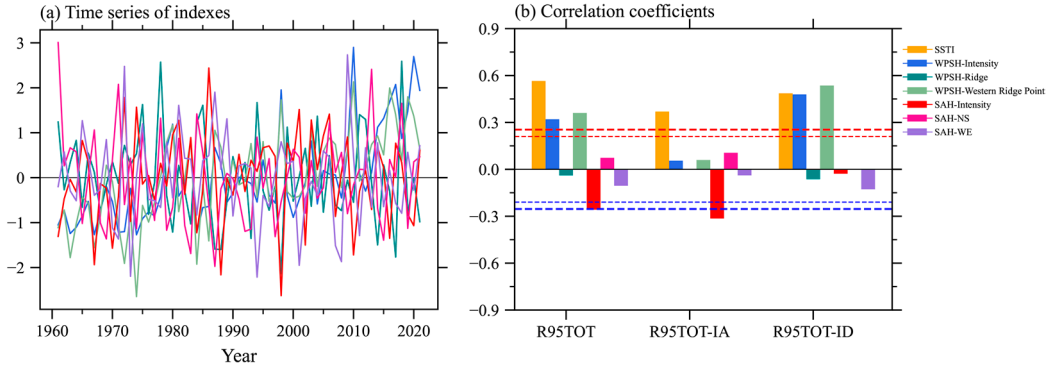

Figure 8. (**a**) Standardized time series of indexes and (**b**) correlation coefficients between original, interannual, and interdecadal R95TOT components and other indexes. Red and blue dashed lines indicate correlations at the 95% and 90% confidence level from 1961 to 2021.

4. Discussion

According to earlier studies, positive western Pacific SST anomalies were responsible for anomalous negative monsoon circulations and a positive WPSH [57]. The correlation coefficients between WPSH intensity and the western ridge point were 0.64 and −0.68 (above the 99% confidence level). In addition, a reduced SAH intensity also correlated with increased western Pacific SST, with a correlation coefficient of −0.27 (above the 95% confidence level). Furthermore, we found that a weakened SAH contributed to the increase in extreme precipitation in NWC, and Ge et al. (2019) showed that this was in accordance with the weakened and apparent heat source over the Tibetan Plateau. Thus, the heat source anomaly is linked to snow cover changes over the Tibetan Plateau [58].

Additionally, we found that the increase in extreme precipitation in NWC showed an interdecadal change in the mid-1980s and accounted for 42% of the total variance of R95TOT. Possible causes for this have been documented, which are closely related to WPSH changes. Particularly, the change in WPSH intensity and the western ridge point induces a greater convergence of moisture transport in NWC [3,34]. Notably, the WPSH significantly enhanced the interdecadal characteristics of extreme precipitation in NWC. Regardless of the upper-tropospheric wave-like teleconnection, the WPSH also affects extreme precipitation in NWC. Consistently, Ding and Wang (2005) found that the circumglobal teleconnection centers are usually barotropic with baroclinic structure and permanent, in which the associated anomalous cyclonic anomaly in Central Asia in Figures 5b and 7b is conducive to the production of extreme precipitation in NWC. This diabatic heating is crucial to maintaining teleconnection, promotes upward motions in NWC, and likely acts as a vital factor in extreme precipitation occurrence, an issue that warrants further study [59].

5. Conclusions

The characteristics and related mechanisms of the interannual variability of summer extreme precipitation in NWC were investigated based on different precipitation products. The selected high-resolution precipitation products showed the main characteristics of the spatial distributions of summer R95TOT and Rx1day in NWC. Both R95TOT and Rx1day generally decreased in a southeast—northwest direction, and there were relatively high values in the Tienshan and Qilian Mountain areas. Notably, the TRMM product underestimated the extremes in the Tienshan mountain areas, which is limited by the application of remote sensing technologies in high-topography areas [50]. In turn, CN05.1 and CPC consistently and accurately described extreme precipitation changes in NWC, whereas the CMIP6 model simulations of the interannual variability of extreme precipitation in NWC were unsuccessful. Therefore, a detailed understanding of the dynamic origins of extreme precipitation in NWC is required.

Atmospheric circulation and related fundamental physical processes are critical for improving modeling and forecasting extreme precipitation. The interannual increased R90TOT in NWC is closely related to a weakened SAH, a strengthened and western-stretched WPSH, enhanced westerly jet, and mid- to high-latitude Rossby wave trains. Rossby wave trains are formed and maintained by SST anomalies in the western Pacific in MJJ. The increased SSTI promotes convection and induces diabatic heating, which triggers an anticyclonic anomaly at the upper level. On the one hand, this anticyclonic anomaly perturbs and enhances the westerly jet, and results in the barotropic Rossby wave train via the Gill-type response. On the other hand, it guides more water vapor convergence to NWC. In addition, mid- to high-latitude Rossby wave trains lead to the configuration of the high-pressure (anticyclonic) anomaly over western Europe and Eastern Asia and a low-pressure (cyclonic) anomaly over Central Asia, which strengthens the water vapor convergence and upward vertical motions to enhance extreme precipitation in NWC.

Supplementary Materials: The following supporting information can be downloaded at: https://www.mdpi.com/article/10.3390/rs15030785/s1, Figure S1: The same as Figure 6 but for SST in JJA; and Figure S2: The same as Figure 7 but for SST in JJA.

Author Contributions: Conceptualization, Q.M.; methodology, Z.L. and H.L.; software, S.W.; validation, Q.M., Z.L. and J.L.; formal analysis, Z.C.; investigation, Q.M.; resources, Q.M.; data curation, Z.L. and H.L.; writing—original draft preparation, Q.M.; writing—review and editing, Z.C.; visualization, Z.L.; supervision, T.S. and G.F.; project administration, G.F.; funding acquisition, Q.M. and G.F. All authors have read and agreed to the published version of the manuscript.

Funding: This research was funded by the National Natural Science Foundation of China (Grant No. 42205023 and No. 42130610).

Data Availability Statement: The original contributions presented in the study are included in the article/supplementary material. Further enquiries can be directed to the corresponding authors.

Acknowledgments: We are grateful to the public data websites for providing the data sets used in this study at no cost. We sincerely thank the reviewers for their insightful comments and useful suggestions as well all our editors for their assistance.

Conflicts of Interest: The authors declare no conflict of interest.

References

1. Li, M.; Ma, Z. Decadal changes in summer precipitation over arid northwest China and associated atmospheric circulations. *Int. J. Climatol.* **2018**, *38*, 4496–4508. [CrossRef]
2. Peng, D.; Zhou, T. Why was the arid and semiarid northwest China getting wetter in the recent decades? *J. Geophys. Res. Atmos.* **2017**, *122*, 9060–9075. [CrossRef]
3. Yang, P.; Xia, J.; Zhang, Y.; Hong, S. Temporal and spatial variations of precipitation in northwest China during 1960–2013. *Atmos. Res.* **2017**, *183*, 283–295. [CrossRef]
4. Li, B.; Chen, Y.; Shi, X.; Chen, Z.; Li, W. Temperature and precipitation changes in different environments in the arid region of northwest China. *Theor. Appl. Climatol.* **2013**, *112*, 589–596. [CrossRef]

5. Shi, Y.; Shen, Y.; Kang, E.; Li, D.; Ding, Y.; Zhang, G.; Hu, R. Recent and future climate change in northwest China. *Clim. Chang.* **2007**, *80*, 379–393. [CrossRef]
6. Hu, Z.; Chen, X.; Chen, D.; Li, J.; Wang, S.; Zhou, Q.; Yin, G.; Guo, M. "Dry gets drier, wet gets wetter": A case study over the arid regions of central Asia. *Int. J. Climatol.* **2019**, *39*, 1072–1091. [CrossRef]
7. Zhang, Y.; Guan, X.; Yu, H.; Xie, Y.; Jin, H. Contributions of radiative factors to enhanced dryland warming over East Asia. *J. Geophys. Res. Atmos.* **2017**, *122*, 7723–7736. [CrossRef]
8. Long, Y.; Xu, C.; Liu, F.; Liu, Y.; Yin, G. Evaluation and projection of wind speed in the arid region of northwest China based on CMIP6. *Remote Sens.* **2021**, *13*, 4076. [CrossRef]
9. IPCC. *Climate Change Impacts, Adaptation and Vulnerability. Fourth Assessment Report of the Intergovernmental Panel on Climate Change*; Cambridge University Press: Cambridge, UK, 2007; Volume 2.
10. Chen, G.; Huang, R. Excitation mechanisms of the teleconnection patterns affecting the July precipitation in northwest China. *J. Clim.* **2012**, *25*, 7834–7851. [CrossRef]
11. Zhang, Y.; Ge, Q.; Liu, M. Extreme precipitation changes in the semiarid region of Xinjiang, northwest China. *Adv. Meteorol.* **2015**, *2015*, 215840. [CrossRef]
12. Alexander, L.V.; Zhang, X.; Peterson, T.C.; Caesar, J.; Gleason, B.; Klein Tank, A.M.G.; Haylock, M.; Collins, D.; Trewin, B.; Rahimzadeh, F.; et al. Global observed changes in daily climate extremes of temperature and precipitation. *J. Geophys. Res. Atmos.* **2006**, *111*, 1042–1063. [CrossRef]
13. Shi, Y.; Shen, Y. Signal, impact and outlook of climatic shift from warm-dry to warm-humid in northwest China. *Sci. Technol. Rev.* **2003**, *2*, 54–57.
14. Lu, S.; Hu, Z.; Yu, H.; Fan, W.; Fu, C.; Wu, D. Changes of extreme precipitation and its associated mechanisms in northwest China. *Adv. Atmos. Sci.* **2021**, *38*, 1665–1681. [CrossRef]
15. Pritchard, H.D. Asia's shrinking glaciers protect large populations from drought stress. *Nature.* **2019**, *569*, 649–654. [CrossRef]
16. Wan, W.; Long, D.; Hong, Y.; Ma, Y.; Yuan, Y.; Xiao, P.; Duan, H.; Han, Z.; Gu, X. A lake data set for the Tibetan Plateau from the 1960s, 2005, and 2014. *Sci. Data* **2016**, *3*, 160039. [CrossRef]
17. Xue, L.; Zhu, B.; Yang, C.; Wei, G.; Meng, X.; Long, A.; Yang, G. Study on the characteristics of future precipitation in response to external changes over arid and humid basins. *Sci. Rep.* **2017**, *7*, 15148. [CrossRef]
18. Chen, F.; Yu, Z.; Yang, M.; Ito, E.; Wang, S.; Madsen, D.B.; Huang, X.; Zhao, Y.; Sato, T.; Birks, H.J.B.; et al. Holocene moisture evolution in arid central Asia and its out-of-phase relationship with Asian monsoon history. *Quat. Sci. Rev.* **2008**, *27*, 351–364. [CrossRef]
19. Chen, F.-H.; Chen, J.-H.; Holmes, J.; Boomer, I.; Austin, P.; Gates, J.B.; Wang, N.-L.; Brooks, S.J.; Zhang, J.-W. Moisture changes over the last millennium in arid central Asia: A review, synthesis and comparison with monsoon region. *Quat. Sci. Rev.* **2010**, *29*, 1055–1068. [CrossRef]
20. Huang, W.; Feng, S.; Chen, J.; Chen, F. Physical mechanisms of summer precipitation variations in the Tarim Basin in northwestern China. *J. Clim.* **2015**, *28*, 3579–3591. [CrossRef]
21. Zhang, J.; Chen, Z.; Chen, H.; Ma, Q.; Teshome, A. North Atlantic multidecadal variability enhancing decadal extratropical extremes in boreal late summer in the early twenty-first century. *J. Clim.* **2020**, *33*, 6047–6064. [CrossRef]
22. Zhang, J.; Ma, Q.; Chen, H.; Zhao, S.; Chen, Z. Increasing warm-season precipitation in Asian drylands and response to reducing spring snow cover over the Tibetan Plateau. *J. Clim.* **2021**, *34*, 1–69. [CrossRef]
23. Chen, Z.; Zhang, J.; Ma, Q.; Li, S.; Niu, M. Multi-timescale modulation of North Pacific Victoria mode on Central Asian vortices causing heavy snowfall. *Clim. Dyn.* **2022**, *2022*, 1–18. [CrossRef]
24. Yin, X.; Zhou, L.-T. Strengthened relationships of northwest China wintertime precipitation with ENSO and midlatitude North Atlantic SST since the mid-1990s. *J. Clim.* **2020**, *33*, 3967–3988. [CrossRef]
25. Wang, H.; Chen, Y.; Pan, Y.; Li, W. Spatial and temporal variability of drought in the arid region of China and its relationships to teleconnection indices. *J. Hydrol.* **2015**, *523*, 283–296. [CrossRef]
26. Hua, L.; Zhong, L.; Ma, Z. Decadal transition of moisture sources and transport in northwestern China during summer from 1982 to 2010. *J. Geophys. Res. Atmos.* **2017**, *122*, 12–522. [CrossRef]
27. Zhao, Y.; Huang, A.; Zhou, Y.; Huang, D.; Yang, Q.; Ma, Y.; Li, M.; Wei, G. Impact of the middle and upper tropospheric cooling over central Asia on the summer rainfall in the Tarim Basin, China. *J. Clim.* **2014**, *27*, 4721–4732. [CrossRef]
28. Wei, W.; Zhang, R.; Wen, M.; Yang, S. Relationship between the Asian westerly jet stream and summer rainfall over central Asia and North China: Roles of the Indian monsoon and the South Asian high. *J. Clim.* **2017**, *30*, 537–552. [CrossRef]
29. Zhou, Y.; Huang, A.; Zhao, Y.; Yang, Q.; Jiang, J.; La, M. Influence of the sea surface temperature anomaly over the Indian ocean in March on the summer rainfall in Xinjiang. *Theor. Appl. Climatol.* **2015**, *119*, 781–789. [CrossRef]
30. Hu, Z.; Zhou, Q.; Chen, X.; Qian, C.; Wang, S.; Li, J. Variations and changes of annual precipitation in Central Asia over the last century. *Int. J. Climatol.* **2017**, *37*, 157–170. [CrossRef]
31. Deng, H.; Chen, Y.; Shi, X.; Li, W.; Wang, H.; Zhang, S.; Fang, G. Dynamics of temperature and precipitation extremes and their spatial variation in the arid region of northwest China. *Atmos. Res.* **2014**, *138*, 346–355. [CrossRef]
32. Cai, Y.; Song, M.; Qian, Z.; Tongwen, W.U.; Luan, C. Reanalyses of precipitation circulation and vapor transportation of severe dry and wet events in summer in arid region of northwest China. *Plateau Meteorol.* **2015**, *34*, 597–610.

33. Chen, D.D.; Dai, Y.J. Characteristics and analysis of typical anomalous summer rainfall patterns in northwest China over the last 50 years. *Chin. J. Atmos. Sci.* **2009**, *33*, 1247–1258.
34. Yao, J.; Chen, Y.; Yang, Q. Spatial and temporal variability of water vapor pressure in the arid region of northwest China, during 1961–2011. *Theor. Appl. Climatol.* **2016**, *123*, 683–691. [CrossRef]
35. Yao, J.; Chen, Y.; Guan, X.; Zhao, Y.; Chen, J.; Mao, W. Recent climate and hydrological changes in a mountain–basin system in Xinjiang, China. *Earth Sci. Rev.* **2022**, *226*, 103957. [CrossRef]
36. Guo, P.; Zhang, X.; Zhang, S.; Wang, C.; Zhang, X. Decadal variability of extreme precipitation days over northwest China from 1963 to 2012. *J. Meteorol. Res.* **2014**, *28*, 1099–1113. [CrossRef]
37. Zhou, L.T.; Huang, R.H. Interdecadal variability of summer rainfall in northwest China and its possible causes. *Int. J. Climatol.* **2010**, *30*, 549–557. [CrossRef]
38. Leung, M.Y.; Zhou, W. Circumglobal teleconnection and eddy control of variation in summer precipitation over northwest China. *Clim. Dyn.* **2018**, *51*, 1351–1362. [CrossRef]
39. Ma, Q.; Zhang, J.; Ma, Y.; Game, A.T.; Chen, Z.; Chang, Y.; Liu, M. How do multiscale interactions affect extreme precipitation in eastern Central Asia? *J. Clim.* **2021**, *34*, 7475–7491. [CrossRef]
40. Wu, J.; GAO, X. A gridded daily observation dataset over China region and comparison with the other datasets. *Chin. J. Geophys.* **2013**, *56*, 1102–1111.
41. Yatagai, A.; Kamiguchi, K.; Arakawa, O.; Hamada, A.; Yasutomi, N.; Kitoh, A. APHRODITE: Constructing a long-term daily gridded precipitation dataset for Asia based on a dense network of rain gauges. *Bull. Am. Meteorol. Soc.* **2012**, *93*, 1401–1415. [CrossRef]
42. Xie, P.; Chen, M.; Yang, S.; Yatagai, A.; Hayasaka, T.; Fukushima, Y.; Liu, C. A gauge-based analysis of daily precipitation over East Asia. *J. Hydrol. Meteorol.* **2007**, *8*, 607–626. [CrossRef]
43. Katiraie-Boroujerdy, P.-S.; Akbari Asanjan, A.; Hsu, K.-l.; Sorooshian, S. Intercomparison of PERSIANN-CDR and TRMM-3B42V7 precipitation estimates at monthly and daily time scales. *Atmos. Res.* **2017**, *193*, 36–49. [CrossRef]
44. Eyring, V.; Bony, S.; Meehl, G.A.; Senior, C.A.; Stevens, B.; Stouffer, R.J.; Taylor, K.E. Overview of the coupled model intercomparison project phase 6 (CMIP6) experimental design and organization. *Geosci. Model Dev.* **2016**, *9*, 1937–1958. [CrossRef]
45. Hersbach, H.; Bell, B.; Berrisford, P.; Hirahara, S.; Horányi, A.; Muñoz-Sabater, J.; Nicolas, J.; Peubey, C.; Radu, R.; Schepers, D.; et al. The ERA5 global reanalysis. *Q. J. R. Meteorol. Soc.* **2020**, *146*, 1999–2049. [CrossRef]
46. Rayner, N.A.; Parker, D.E.; Horton, E.; Folland, C.K.; Alexander, L.V.; Rowell, D.; Kent, E.C.; Kaplan, A. Global analyses of sea surface temperature, sea ice, and night marine air temperature since the late nineteenth century. *J. Geophys. Res. Atmos.* **2003**, *108*, 4407. [CrossRef]
47. Demšar, U.; Harris, P.; Brunsdon, C.; Fotheringham, A.S.; McLoone, S. Principal component analysis on spatial data: An overview. *Ann. Assoc. Am. Geogr.* **2013**, *103*, 106–128. [CrossRef]
48. Huang, G.; Qu, X.; Hu, K. The impact of the tropical Indian ocean on South Asian high in boreal summer. *Adv. Atmos. Sci.* **2011**, *28*, 421–432. [CrossRef]
49. Sui, C.H.; Chung, P.; Li, T. Interannual and interdecadal variability of the summertime western North Pacific subtropical high. *Geophys. Res. Lett.* **2007**, *34*, 1–6. [CrossRef]
50. Trenberth, K.E. Climate diagnostics from global analyses: Conservation of mass in ECMWF analyses. *J. Clim.* **1991**, *4*, 707–722. [CrossRef]
51. Takaya, K.; Nakamura, H. A formulation of a phase-independent wave-activity flux for stationary and migratory quasigeostrophic eddies on a zonally varying basic flow. *J. Atmos. Sci.* **2001**, *58*, 608–627. [CrossRef]
52. Sun, F.; Chen, Y.; Li, Y.; Li, Z.; Duan, W.; Zhang, Q.; Chuan, W. Incorporating relative humidity improves the accuracy of precipitation phase discrimination in High Mountain Asia. *Atmos. Res.* **2022**, *271*, 106094. [CrossRef]
53. Yin, X.; Zhou, L.T. Enhanced moisture transport associated with the interdecadal change in winter precipitation over northwest China. *Int. J. Climatol.* **2022**, *42*, 385–399. [CrossRef]
54. Wallace, J.M.; Gutzler, D.S. Teleconnections in the geopotential height field during the northern hemisphere winter. *Mon. Weather Rev.* **1981**, *109*, 784–812. [CrossRef]
55. Zhihong, J.; Jinhu, Y.; Qiang, Z. Influence study on spring Indian ocean SSTA to summer extreme precipitation events over the eastern part of northwest China. *J. Tropical Meteorol.* **2009**, *25*, 641–648.
56. Zhu, Z.; Lu, R.; Yan, H.; Li, W.; Li, T.; He, J. Dynamic origin of the interannual variability of West China autumn rainfall. *J. Clim.* **2020**, *33*, 9643–9652. [CrossRef]
57. Cha, D.H.; Jin, C.S.; Lee, D.K. Impact of local sea surface temperature anomaly over the western North Pacific on extreme East Asian summer monsoon. *Clim. Dyn.* **2014**, *37*, 1691–1705. [CrossRef]
58. Ge, J.; You, Q.; Zhang, Y. Effect of Tibetan Plateau heating on summer extreme precipitation in eastern China. *Atmos. Res.* **2019**, *218*, 364–371. [CrossRef]
59. Ding, Q.; Wang, B. Circumglobal teleconnection in the northern hemisphere summer. *J. Clim.* **2005**, *18*, 3483–3505. [CrossRef]